THE ANALYSIS OF 3D MODEL CHARACTERIZATION AND ITS IMPACT ON THE ACCURACY OF SCATTERING CALCULATIONS

A. D. Hellicar

CSIRO ICT Centre
P. O. Box 76, Epping, NSW 1710, Australia

J. S. Kot

BAE Australia
40–52 Talavera Road, North Ryde 2113, NSW, Australia

G. C. James

CSIRO ICT Centre
P. O. Box 76, Epping, NSW 1710, Australia

G. K. Cambrell

Clayton Campus
Monash University, Wellington Road, VIC 3800, Australia

Abstract—When employing computational methods for solving problems in electromagnetic scattering the resulting solutions are strongly determined by the geometry of the scatterer. Careful consideration must therefore be given to the computational geometry used in representing the scatterer. Here we show that the solution for a problem as simple as plane wave scattering off a PEC sphere is sensitive to the computational geometry used to represent the sphere. We show this by implementing 4 higher-order computational geometry schemes over 3 different tessellations resulting in 45 different representations of the sphere. Two methods for solving the scattering problem are implemented: the boundary-element method (BEM) based on the MFIE, and the physical optics (PO) method. Results are compared and insights are obtained into the performance of the various schemes to model surfaces accurately and efficiently. The comparison of the

different schemes takes into consideration the required computational resources in implementing the schemes. Some unexpected results are discovered and explanations given.

1. INTRODUCTION

Computational electromagnetism (CEM) involves geometric modelling of objects which interact with an electromagnetic field. To represent arbitrary shapes, mesh discretization is commonly used to decompose the domain of the problem into discrete sub-domains, either volume elements as in the finite-element method (FEM) or finite volume method, or surface patches as in the boundary-element method (BEM), the method of moments or the physical optics (PO) method. This approach allows the use of higher-order computational geometric schemes to represent the shapes of objects, but these schemes carry the penalty of additional computational effort, and so the relative computational efficiency of higher-order schemes over simple schemes is a matter of practical interest. In this paper we will consider the solution of the electromagnetic scattering problem using BEM and PO, where computational geometry is used to represent the surface of a scatterer, and compare the efficiency of a number of different schemes.

A number of geometric representations have been employed in solving scattering problems. Rao et al. [1] implemented basis functions on a flat-facetted representation of the scatterer. Wandzura [2] implemented basis functions on curvilinear patches. Graglia et al. [3] developed higher-order bases and Wang and Webb [4] developed adaptive bases, both on curvilinear patches. Second-order polynomial patch representations were commonly employed in these papers and the wider literature. In [5], a double higher order method is introduced which allows the order of the geometry surface currents representations to be independently increased. [5] showed that both higher-order geometries and currents are required to take advantage of improved convergence.

NURBS surfaces, which are higher-order and rational patch representations, have also been employed in solving scattering problems using the BEM [6] and PO [7]. Exact spherical representations have also been used in solving scattering problems. For example [8] projects a cubic tessellation onto the sphere.

This paper examines the effect of the geometric representation upon solution accuracy by implementing a number of geometric representations from computer aided graphics design (CAGD). These representations include interpolatory, Bezier and Rational Bezier

expressions from flat facetted first-order through to fourth-order curvilinear patches. These geometric representations have been implemented using a common basis that allows a direct comparison of the efficiency of the various representations. Also, by using rational geometrical representations, the test problem analysed is solved with a method that exactly represents the problem's geometry, and allows the geometric errors incurred in the remaining representations to be separated from the solution method errors.

This paper differs from the work in [5] in that the spherical geometry considered there inscribe the sphere and contain creases; here a case of a geometry which eliminates the creases is included along with further cases which span the spheres surface. [8] implements an exact representation of the sphere by projecting a cube onto the sphere. This results in a formulation that is not rational polynomial due to a square root in the expression for the surface. Here an exact representation of the sphere is implemented in a rational polynomial form. Computational geometry based on rational polynomials are of interest because they are used in NURBS for describing a wide class of surfaces. Here, the exact representation of a sphere is a special case of a general computational geometry.

The geometric model used affects the accuracy of the solution in two ways: firstly how closely the computational model represents the actual surface of the object directly affects the solution; and secondly, because the basis used to approximate the unknown surface currents is supported on the surface patches, the differential geometry of the surface patch affects the accuracy of the interpolation used to represent the currents. A simple example of the latter effect is the reduction in accuracy caused in the FEM by so-called slivers, or elements with very small internal angles [9]. In [10], we have compared the performance of different higher-order bases in the BEM using an exact geometrical representation of the surface of the scatterer. Here, we examine the more general case where both surface geometry and surface current are approximated at different orders. The surface current is approximated using the interpolatory vector basis introduced in [11], which is convenient for both the BEM and PO methods.

Finally, we would like to emphasise that geometrical representations can be improved by a procedure of mesh or h-refinement, thereby reducing the total curvature in a patch thus reducing the influence of the geometry representation on the solution. However, the authors have focussed on highly curved patches to highlight the issues when dealing with cases where curvature cannot be reduced, or is unavoidable due to the use of large patches with higher-order basis functions.

2. SCHEMES FOR REPRESENTING SURFACES

Both the BEM and PO techniques require a computational representation of the scatterer's surface. The surface is represented by a tessellation of T patches that partition the scatterer's surface. Here triangular patches are employed, and each patch is parameterised by homogeneous ζ coordinates such that $\vec{\zeta} = (\zeta_1, \zeta_2, \zeta_3)$, $\zeta_1 + \zeta_2 + \zeta_3 = 1$ and $0 \leq \zeta_i \leq 1$ where $i = 1, 2, 3$. These ζ coordinates then form a parameterisation of the triangular region of the plane in the positive octant of three dimensional ζ space with vertices $\vec{\zeta} = (1, 0, 0)$, $\vec{\zeta} = (0, 1, 0)$, $\vec{\zeta} = (0, 0, 1)$. The position vector on the tth surface patch is then $\vec{r}_t(\vec{\zeta})$, $t \in \{1 \cdots T\}$, see Fig. 1. The Jacobian J of the mapping is $J = |(\frac{\partial \vec{r}}{\partial \zeta_{i+1}} - \frac{\partial \vec{r}}{\partial \zeta_i}) \times (\frac{\partial \vec{r}}{\partial \zeta_{i+2}} - \frac{\partial \vec{r}}{\partial \zeta_i})|$, where index arithmetic is modulo 3.

The common method for representing patches is to employ a set of points whose locations completely control the patch location and curvature. Each of these control points has a scalar basis function associated with it. The basis functions are parameterised in terms of $\vec{\zeta}$ which then forms a parameterisation of the position vector over the patch. Higher-order representations require a larger number of basis functions and associated control points. The expression for the position vector over an order p polynomial patch is then:

$$\vec{r}_t\left(\vec{\zeta}\right) = \sum_{|I|=p} B_{[I]}\left(\vec{\zeta}\right) \vec{P}_{t,[I]} \tag{1}$$

where $B_{[I]}(\vec{\zeta})$ are basis functions attached to each control point $\vec{P}_{t,[I]}$, associated with patch t. For triangular patches $[I] = [I_1, I_2, I_3]$ is a multi-index such that $|I| = I_1 + I_2 + I_3$ and $0 \leq I_j \leq p$, $j = 1, 2, 3$. In the CAGD community, Bézier patches are often employed as the
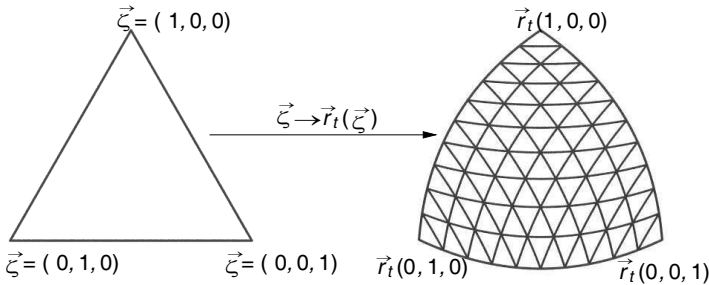

Figure 1. Mapping from homogeneous ζ coordinates onto curvilinear $\vec{r}_t$ patch.

choice of geometric basis function.

The Bézier patch basis functions are of the form:

$$B_{[I]}\left(\vec{\zeta}\right) = \frac{(I_1 + I_2 + I_3)!}{I_1!I_2!I_3!} \zeta_1^{I_1} \zeta_2^{I_2} \zeta_3^{I_3}. \tag{2}$$

Alternatively Lagrange interpolation basis functions can be used which are of the form

$$B_{[I]}\left(\vec{\zeta}\right) = \Pi_{j=1}^3 \left[\frac{1}{I_j!} \Pi_{k=0}^{I_j-1} \left(p\zeta^j - k\right) \right]. \tag{3}$$

It should be noted that both Bézier and Lagrange basis functions form polynomial geometric representations complete to order p, and hence there is a one to one mapping of any pth order geometry generated by Bézier patches to any interpolated geometry. The difference between these representations is the locations of the respective control points. Bézier control points allow for easy control of a patch's location and boundary tangent planes, whereas interpolatory control points force the patch location to match the spatial location of the control points at associated values of the parameterisation.

Further to the polynomial representation given in Eq. (1), rational representations are often used in CAGD to achieve more refined control over surface positioning. The expression for a pth order rational representation is:

$$\vec{r}_t\left(\vec{\zeta}\right) = \frac{\sum_{|I|=p} B_{[I]}\left(\vec{\zeta}\right) \vec{P}_{t,[I]}^x}{\sum_{|I|=p} B_{[I]}\left(\vec{\zeta}\right) P_{t,[I]}^w} \tag{4}$$

where the control points for patch t are now represented in terms of a spatial vector part $\vec{P}_{t,[I]}^x$ and a scalar weight $P_{t,[I]}^w$. An advantage of rational Bézier patches is that they allow exact representation of quadric surfaces [12], which form a particularly important class of surfaces in electromagnetic scattering. For any given order p, polynomial and rational representations have an identical number of control points and basis functions defining the surface; however, the polynomial control points have three components in comparison to the rational control point's four components.

Here, four different schemes for generating patch approximations are employed. The notation σ_{pah} is used to define the structure of the tessellation representing the surface geometry. σ refers to the form of the surface representation. The surface analysed in this paper is restricted to a spherical PEC. Three (parent) tessellations were employed for representing the spherical surface. These tessellations are unique: a single curvilinear equilateral patch may be rotated and

translated to generate all patches within a tessellation. This allows the effect of increasing the number of patches to be studied without reducing the quality (increase in variation of angles) of the patches, which is the case for curvilinear h-refined tessellations containing non-equilateral patches. The three parent tessellations are based on the three triangular Platonic solids, the tetrahedron, octahedron and icosahedron. In referring to a specific tessellation the σ is replaced by tet, oct or ico depending on the parent tessellation.

p indicates the order of the representation (notwithstanding the special case of σ_{3th} discussed later), a can take on values i, t, o, r and refers to which scheme is used to generate the patch, and h is the level of h-refinement used. The various schemes are outlined below.

2.1. Interpolatory-σ_{pih}

The interpolatory scheme uses simple Lagrange interpolation to approximate the surface at a set of points $\vec{r}_t(\vec{\zeta}^{[I]})$, where, for a pth order representation

$$\vec{\zeta}^{[I]} = \left\{ \frac{I_1}{p}, \frac{I_2}{p}, \frac{I_3}{p} \right\}$$

Geometries of up to fourth-order are implemented. The four approximations can be seen on the left side of Fig. 2.

2.2. Vertex Tangent Approximation-σ_{pth}

The vertex tangent approximation represents surfaces at the patch vertices. The first-order version (σ_{1th}) interpolates the surface at the patch vertices, and hence is identical to the first-order interpolatory scheme.

The second-order version (σ_{2th}) exactly matches the vertex locations and the vertex tangent planes. This can be seen in the top left plot in Fig. 3 where the surface normal vectors (which are plotted on both sides of one edge) are identical at both ends of the edge.

Finally a third representation (σ_{3th}) exactly represents the vertex location, vertex tangent plane and all vertex tangent plane derivatives along the patch edges, such that the generated patch exactly matches that of the desired surface along the three edges. This can be seen in the top right of Fig. 3 where the oct_{3t1} surface normals match at the vertices and the patch boundaries are exact circular arcs.

It should be noted that σ_{3th} is the only geometry where p does not correspond to the order of the representation. Although $p = 3$, a second order rational representation is used to enforce the high-order tangent plane derivatives at the patch vertices. Note that the control points
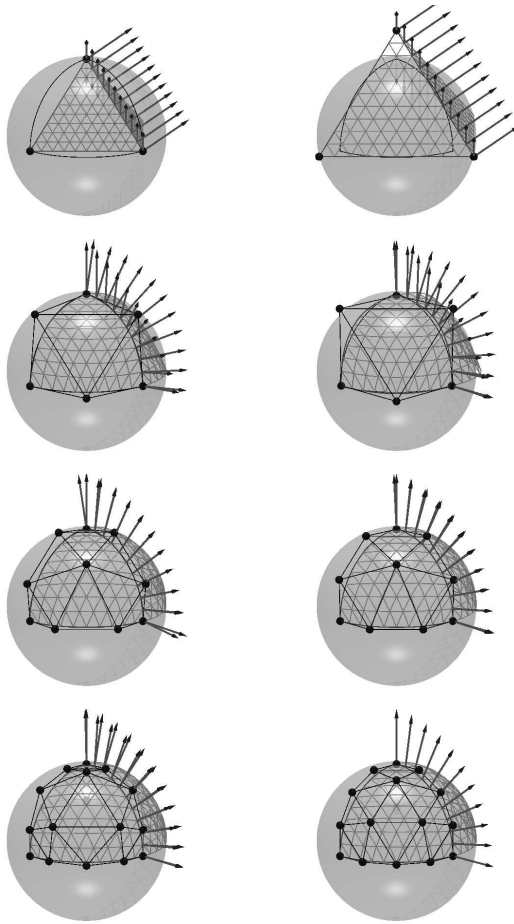
Figure 2. Bézier control points for a patch, two adjacent generated patches and surface normal vectors on each side of the patch's shared edge for various geometries. Left: oct_{pi1} scheme. Right: oct_{po1} scheme.

required to generate the vertex tangent plane behave differently from those used in the second order optimised rational expression discussed below in σ_{prh}.

2.3. Optimised Polynomial-σ_{poh}

The optimised polynomial representation uses control points that minimise the error in approximating the surface in terms of the position
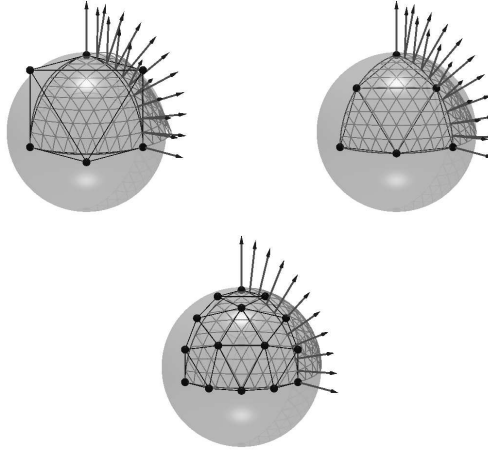
Figure 3. Bézier control points for a patch, two adjacent generated patches and surface normal vectors on each side of the patches' shared edge for various geometries. Top left: oct_{2t1}. Top right: oct_{3t1}. Bottom: oct_{4r1}.

vector. Because the test problem solved employs a unit spherical scatterer, the optimisation minimizes the following cost function:

$$f = \int_{S_2} ||\vec{r}_t(\zeta)| - 1| \ d\vec{\zeta} \tag{5}$$

The optimised scheme's control points and patches are shown on the right of Fig. 2. Whereas the first-order interpolatory scheme generates an octahedron inscribed within the sphere, the optimised scheme increases the octahedron outside the structure the minimise the error. Similarly it is noted that optimisation of the surface generates surface normals that more closely match across the edges as seen by comparing the fourth-order schemes at the bottom of Fig. 2.

2.4. Optimised Rational-σ_{prh}

The optimised rational representation minimizes the same cost function above, but employs a rational representation for $\vec{r}_t$. The fourth-order optimised rational scheme is shown at the bottom of Fig. 3. The oct_{4r1} patch is an exact representation of a spherical patch.

3. TEST PROBLEM

The problem selected for comparing the geometries is the case of a PEC sphere of radius a illuminated by an incident linearly polarised time-harmonic plane wave of wavenumber k (Fig. 4).

Initially the ability of the various geometric representations at approximating the scatterer geometry was examined. Two measures of each scheme's ability to model the surface were calculated by integrating both the error in surface position, and the error in tangent plane orientation, across the entire surface. The position error E_r and tangent plane error E_n are given by:

$$E_r = \sqrt{\int_\sigma \frac{(|\vec{r}| - 1)^2}{4\pi} d\sigma} \tag{6}$$

$$E_n = \sqrt{\int_\sigma \frac{|\vec{r} \times \vec{n}(\vec{r})|^2}{4\pi} d\sigma} \tag{7}$$

where $\vec{n}(\vec{r})$ is the normal vector generated by the computational geometry.

Having calculated the geometric errors due to the various representations, the next step was to calculate the errors that the schemes introduced into a CEM solution.
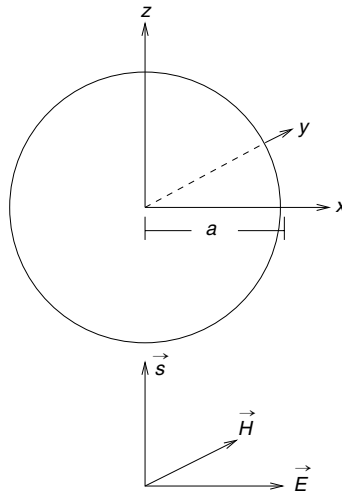

Figure 4. Problem geometry with PEC sphere of radius a illuminated by incident time harmonic plane wave with electric field polarised in x direction.
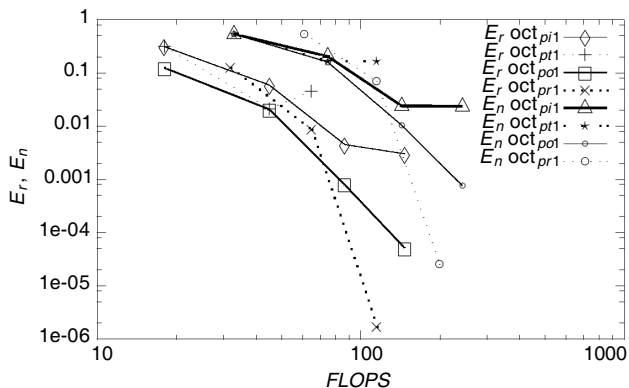
Figure 5. E_r and E_n against FLOPS for oct_{pa1} schemes.

A PO solution and a BEM solution of the MFIE were employed in calculating the equivalent surface currents produced by the scattering problem.

4. THE PHYSICAL OPTICS METHOD

The method of Physical Optics defines the equivalent surface currents as those currents satisfying an approximate boundary condition at each point on the surface. The boundary condition is approximate in the sense that the surface at the point is assumed to be infinite and planar at each point, and thus the planar boundary conditions are used. In general an analytic or numerical representation of the geometry may be used, the only requirement being that an integration rule can be constructed for allowing integration of the equivalent currents in calculating the scattered field. Here, standard cubature rules on triangular patches are implemented [13]. The tessellations of triangular patches employed in representing the scatterer in the BEM solution are also employed in representing the scattering the PO solution. This allows the sensitivity of the two algorithms to the various representations to be compared.

For a PEC scatterer the PO solution involves calculating the surface currents directly as:

$$\vec{J}_s(\vec{r}) = \begin{cases} 2\vec{n}(\vec{r}) \times \vec{H}^{inc}(\vec{r}) & \vec{r} \in \sigma_i \\ 0 & \vec{r} \in \sigma_s \end{cases} \tag{8}$$

where σ_i is the region directly illuminated by the incident planewave,

and σ_s is the shadow region. The error in the RCS is calculated as:

$$\tilde{E}_{PO} = \left[\sum_{\vec{s} \in \{v,e,c\}} \int_{k_1}^{k_2} \frac{(RCS_{PO} - RCS_{calc})^2}{3(k_2 - k_1)} dk \right]^{\frac{1}{2}} \tag{9}$$

where $\vec{s} \in \{v, e, c\}$ refers to the direction of propagation that is incident on a patch vertex, edge midpoint, or centre respectively. RCS_{PO} results when calculating the Radar Cross Section by the Physical Optics method using an analytic formulation of the currents in (9) over a sphere. The reason for averaging over the three rotations can be seen in Figs. 6 and 7. Fig. 6 shows the oct_{2i1} tessellation from the three directions of propagation $\vec{s} \in \{v, e, c\}$. Fig. 7 shows the resulting RCS dependancy on the direction of propagation.

   The limits of integration in (9) are $k_1 = 0.04\pi$, $k_2 = 3\pi$. It should be noted that normally the Physical Optics solution would not be
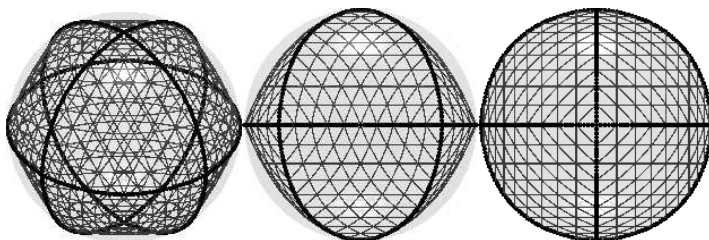

Figure 6. Three oct$_{2i1}$ orientations. Left: face centered. Center: Edge centered and Right: Vertex centered.
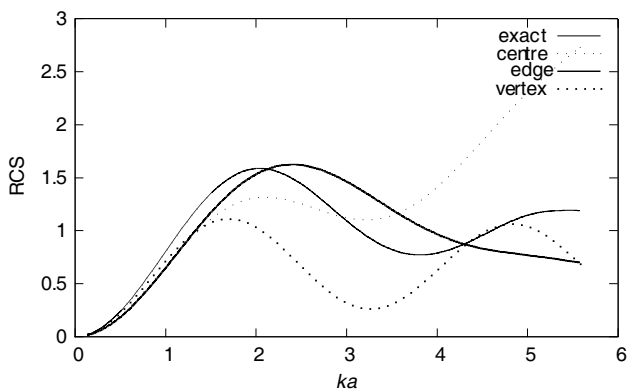

Figure 7. Physical optics normalised monostatic RCS for oct$_{2i1}$ for face centered, edge centered and vertex centered orientations.

applied in the low frequency regime; however, from the perspective of examining the accuracy of the geometric representations, it is informative to study a wider frequency range. This is motivated by the fact that in the full BEM solution (which applies in the lower frequency regime, described in the following Section) the surface current can be expressed in terms of the PO current plus a correction term derived from the MFIE (10).

5. THE BOUNDARY ELEMENT METHOD

The BEM involves solving a boundary integral equation (BIE) which relates the incident field to the equivalent currents defined over the surface of the scatterer. The BEM is typically solved by partitioning the scatterer's surface geometry into a tessellation of patches. A set of vector basis functions are then deployed over these patches. The BIE solved here is the Magnetic Field Integral Equation (MFIE) which is suitable for solving scattering by closed PEC objects. The MFIE over a PEC surface σ [14] is of the form:

$$\vec{n}(\vec{r}) \times \vec{H}^{inc}(\vec{r}) = \frac{1}{2}\vec{J}_s(\vec{r}) + \vec{n}(\vec{r}) \times \fint_{\sigma(\vec{r}')} \vec{J}_s(\vec{r}') \times \nabla'\phi(\vec{r},\vec{r}')d\sigma(\vec{r}'), \tag{10}$$

where $\vec{n}$ is the surface normal, $\vec{H}^{inc}$ the known incident magnetic field, $\vec{J}_s$ the unknown equivalent surface current, $\fint$ corresponds to a Cauchy principal value integral and ϕ is the scalar Helmholtz Green's function in free space:

$$\phi(\vec{r},\vec{r}') = \frac{e^{-jkr}}{4\pi r}, \tag{11}$$

where $r = |\vec{r} - \vec{r}'|$ is the separation between field point $\vec{r}$ and source point $\vec{r}'$. In solving the MFIE the unknown currents are expanded in a set of basis functions [11] of the form:

$$\vec{f}^i_{[I]}\left(\vec{r}\left(\vec{\zeta}\right)\right) = B_{[I]}\left(\vec{\zeta}\right)\vec{n}\left(\vec{r}\left(\vec{\zeta}\right)\right) \times \vec{a}^i_{[I]} \tag{12}$$

where $\vec{f}^i_{[I]}(\vec{r})$ is one of two basis functions ($i = 1, 2$) associated with an interpolating node $[I]$. $B_{[I]}(\vec{\zeta})$ are the Lagrange interpolatory basis functions, and $\vec{a}^i_{[I]}$ is one of two ($i = 1, 2$) orthonormal vectors perpendicular to the average surface normal at node $[I]$. This results in a set of vector basis functions $\vec{f}_j$, $j \in 1 \cdots N$, where $N = 2G$ and G is the total number of interpolating nodes over the tessellation. It should be noted that the surface current expressions for the BEM and

PO solutions is a point of difference. The BEM currents are expanded over a basis in (12), whereas the PO currents are defined directly in (8).

Solution proceeds by expanding the surface current $\vec{J}_s$ over the set of vector basis functions $\vec{f}_j$ such that

$$\vec{J}_s(\vec{r}) = \sum_{j=1}^{N} F^j \vec{f}_j(\vec{r}). \tag{13}$$

A point matching technique is employed where the MFIE (10) is enforced at a set of field points $\vec{r}_i$, and the resulting system of equations:

$$\vec{n}(\vec{r}_i) \times \vec{H}^{inc}(\vec{r}_i)$$

$$= \sum_{j=1}^{N} F^j \left[\frac{1}{2} \vec{f}_j(\vec{r}_i) + \vec{n}(\vec{r}_i) \times \oint_{\sigma(\vec{r}')} \vec{f}_j(\vec{r}') \times \nabla' \phi(\vec{r}_i, \vec{r}') d\sigma(\vec{r}') \right]. \tag{14}$$

is solved for the unknown coefficients F^j.

The integrand in 14 is singular for the case of the field point $\vec{r}_i$ existing within the support of the basis function $\vec{f}_j(\vec{r}')$. For singular cases numerical evaluation proceeds by applying Duffy's transformation [15] and then standard Gauss-Legendre cubature rules. For non-singular cases standard triangular numerical cubature rules are employed [13].

The calculated surface currents $\vec{J}_s$ are compared with the analytic Mie series solution $\vec{J}_{Mie}$ [16]. The Mie series solution was calculated using software [17]. Two error values are calculated:

(i) E_{RMS}
The surface current RMS error is calculated by integration over the entire spherical surface.

$$E_{RMS} = \sqrt{\frac{\int_\sigma \left| \vec{J}_s - \vec{J}_{Mie} \right|^2 d\sigma}{\int_\sigma \left| \vec{J}_{Mie} \right|^2 d\sigma}} \tag{15}$$

(ii) E_{RCS}
The numerical normalised RCS (RCS_J) is calculated from the computed surface currents $(\vec{J}_s)$ and compared with the analytic normalised Mie series RCS (RCS_{Mie}):

$$E_{RCS} = \frac{|RCS_J - RCS_{Mie}|}{RCS_{Mie}}. \tag{16}$$

Both E_{RMS} and E_{RCS} are calculated at a single frequency. To eliminate the possibility of uncharacteristically low errors in the RCS caused by cross overs at various frequencies in the numerical and analytic plots, averaged values of these measures are generated. Frequency averaged results $\tilde{E}_{RMS}$ and $\tilde{E}_{RCS}$ are calculated across a range of frequencies $0.1 < ka < 2.5$ from E_{RMS}, E_{RCS} respectively. Sample frequencies over which E_{RMS} and E_{RCS} are averaged are logarithmically distributed throughout the frequency range.

6. RESULTS

Each of the schemes outlined in Section 2 were applied to the three problems described in Sections 3, 4 and 5.

Initially each scheme was tested for its accuracy at representing the spherical scatterer. Fig. 5 plots E_r (6) and E_n (7) errors for the oct_{pa1} schemes against the number of floating point operations (FLOPS). All plots against FLOPS in this paper are plotted against the number of FLOPS each scheme requires to calculate a surface point, with the exception of the E_n plot in Fig. 5 which is plotted against FLOPS to calculate a tangent vector. The values are shown in Table 1, where multiplication and addition type operations use 1 FLOPS and division 3 FLOPS.

The PO technique was then applied to each scheme. Fig. 7 plots the RCS for three different orientations of the geometry which are

Table 1. Total number of flops and storage bytes required to compute operations used by the various computational geometric representations. P_{flops}: flops to calculate position vector, V_{flops}: flops to calculate tangent vector.

Computational Metrics across Geometric Representations				
ID	p	P_{flops}	V_{flops}	Memory (bytes)
σ_{1ih}, σ_{1oh}, σ_{1th}	1	18	33	72
σ_{2ih}, σ_{2oh}, σ_{2th}	2	45	75	144
σ_{3ih}, σ_{3oh}	3	87	143	240
σ_{4ih}, σ_{4oh}	4	147	243	360
σ_{1rh}	1	32	61	96
σ_{2rh}, σ_{3th}	2	65	115	192
σ_{3rh}	3	115	199	320
σ_{4rh}	4	185	319	480

shown in Fig. 6. Fig. 8 plots the rotation and frequency averaged RCS errors $\tilde{E}_{PO}$ (9) against FLOPS.

Finally the schemes were employed in a BEM solution. Figs. 9 and 10 show the average RMS error in surface currents $\tilde{E}_{RMS}$ and the average error in the RCS $\tilde{E}_{RCS}$ respectively. Both plots give the result against FLOPS where a fourth-order representation is employed for the surface currents. Fig. 11 compares the order of the surface current bases. E_{RMS} is plotted for both first-order and fourth-order surface current representations on all three parent tessellations against FLOPS. Fig. 12 illustrates the variation of the surface current RMS error against frequency for fourth-order currents on oct_{4a1} tessellations.
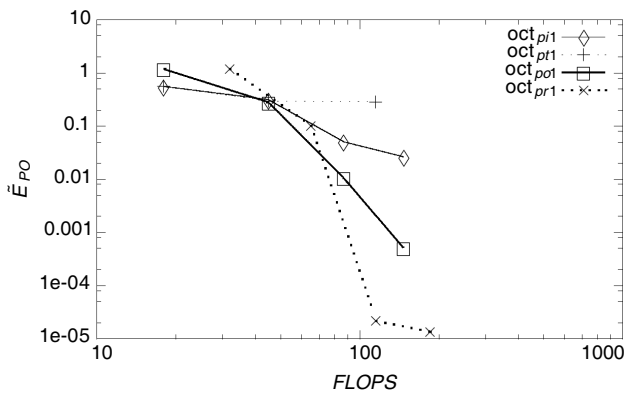

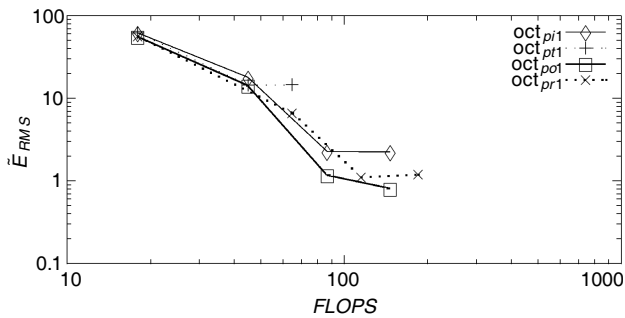**Figure 8.** $\tilde{E}_{PO}$ incurred by oct_{pa1} tessellations.

Figure 9. $\tilde{E}_{RMS}$ incurred by fourth-order surface currents over oct_{pa1} tessellations against $FLOPS$ for the BEM solution.
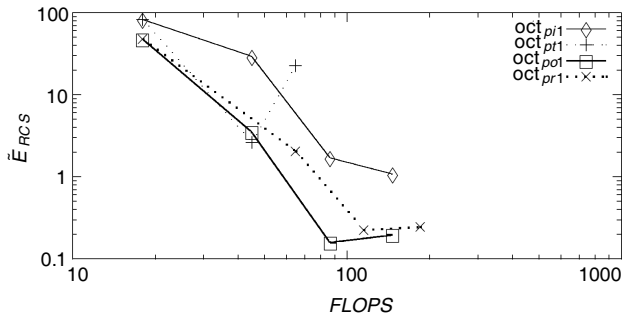
Figure 10. $\tilde{E}_{RCS}$ incurred by fourth-order surface currents over oct_{pa1} tessellations against $FLOPS$ for the BEM solution.
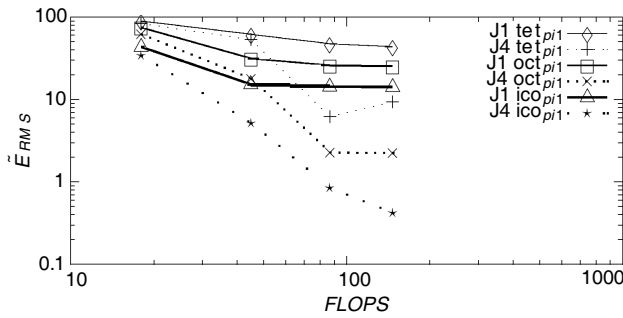

Figure 11. $\tilde{E}_{RCS}$ incurred by both first- and fourth-order surface current basis functions over σ_{pi1} tessellations against $FLOPS$ for the BEM solution.
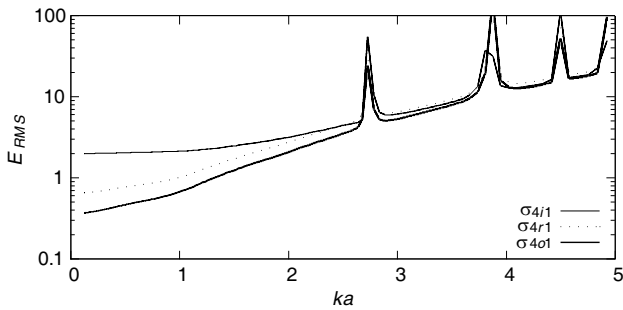

Figure 12. E_{RMS} of various fourth-order geometry representations against frequency for the BEM solution.

7. DISCUSSION OF RESULTS

The results shown in Section 6 give a number of insights into the factors affecting the accuracy of the methods used.

The spherical approximation problem results illustrate that position vector and tangent plane error distributions are similar. Both these characteristics (plotted in Fig. 5) are of interest in CEM as they specify the allowable distributions of the surface current. Not surprisingly higher-order representations yield more accurate approximations of both the position vector and tangent plane, with rational representations outperforming the polynomial schemes.

The Physical Optics results in Fig. 8 show a similar behaviour to those of the geometry approximation results. Interestingly the exact spherical scheme (oct_{4r1}) yields an error of the order 10^{-5}. It should be noted that this error should be zero, and this defines the error floor for the PO solution due to limitations in the accuracy of the numerical cubature employed to calculate the Radar Cross Section.

The BEM is solved using the geometries from the various schemes and results for the errors in equivalent surface currents and RCS were given in Figs. 9 and 10. The surface current errors are similar to those of the errors in the RCS, although the interpolation scheme's error is relatively larger in the RCS calculation. It should be noted from Fig. 5 that the interpolation scheme approximation contains tangent planes which are relatively close to those of the optimised and rational schemes, whereas the interpolation approximation generates surfaces with relatively larger position errors than the optimised or polynomial and rational schemes. It seems that the surface current error in Fig. 9 is closely related to the tangent plane error whereas the RCS error is closely related to the position errors. This is not surprising, as in calculating the error in surface currents the orientation of the currents is compared, whereas in calculating the RCS any change in the cross sectional area produced by the intersection of the scatterer and the plane orthogonal to the direction of propagation produces a change in the high frequency RCS limit.

To compare the utility of the various higher-order geometries for both low and high order surface current representations, the BEM was solved for first and fourth-order basis functions. These results are plotted in Fig. 10. These results clearly indicate that the benefits of higher-order geometrical approximations are only realized for higher-order currents. There is minimal benefit in increasing the order of the geometry beyond second-order for first-order currents.

The interpolation scheme along with the optimised polynomial and rational schemes are compared in the frequency domain in Fig. 12.

Resonant error behaviour is noted for ka value around 2.744 which corresponds to the first of the spurious cavity solutions [18].

Of interest is the relative ability of the various schemes to approximate the geometry and solve the BEM and PO problems. Of the interpolatory, optimised polynomial and rational schemes, the interpolatory scheme always generates the larger errors. The optimised rational scheme is more accurate for the geometry approximation and PO problems, whereas the optimised polynomial scheme is better at solving the BEM. In particular the question arises as to why the fourth-order rational scheme, which exactly represents the sphere, incurs larger errors than the approximate representation produced by the fourth-order optimised polynomial scheme (10^{-4} RMS position error). It would be expected that the optimised rational representation BEM solution error has no component due to the error in representing the scattering geometry, and hence would yield solutions with lower errors than the optimised polynomial scheme; however, this is clearly not the case as can be seen in Fig. 12 across the entire frequency range in question. The reason for this result lies in the quality of the parameterisation of the surface, not the surface accuracy itself. The variation in the Jacobian of the optimised polynomial patch over the patch is much less than the variation of the generated optimised rational patch. This is seen in Table 2, where the ratio of maximum to minimum Jacobian values are given for the three fourth-order schemes. The ordering of the schemes in terms of variation in the Jacobian corresponds to the ordering of the schemes in terms of accuracy of the solution. This is not surprising, given that completeness of the surface current representation to a given order for the Bézier and Lagrange interpolating polynomials holds on the parameterisation domain ($\vec{\zeta}$). When these polynomials are mapped onto the problem domain a distorted mapping will yield more accurate representations in regions where the mapping is compressed, and less accurate representations where the mapping is stretched. Completeness in the problem domain holds only where the Jacobian is constant across the patch. Therefore the more regular mapping of

Table 2. Ratio of maximum to minimum Jacobian values on σ_{ra1} patches.

	tet$_{4a1}$	oct$_{4a1}$	ico$_{4a1}$
σ_{4i1}	3.4902	1.7964	1.2470
σ_{4r1}	3.5710	1.7489	1.2357
σ_{4o1}	1.6366	1.2375	1.0614

the optimised polynomial scheme generates a more evenly distributed set of basis functions which are more able to represent the solution currents.

8. CONCLUSION

This paper has presented a number of schemes for approximating geometries in computational electromagnetics. Three test problems were introduced to analyse the capability of the schemes, a geometric approximation, and BEM and PO solutions. For the presented schemes approximating spheres of size $ka < 5$ it appears that the geometrical errors are highly correlated with the PO and BEM errors. As expected geometric errors do have an effect on the solution accuracy for these computational electromagnetic methods.

For the patch curvatures considered in this paper and first-order currents, low order geometries ($p = 2$) are adequate for representing the geometry. For higher-order currents, benefits are realised by increasing the geometrical representation beyond $p = 2$.

For geometry approximation and PO problems the interpolatory scheme is worse than the optimised polynomial scheme which in turn is worse than the optimised rational scheme as might be expected.

For the BEM the optimised rational scheme was worse than the optimised polynomial scheme and this was not expected. It was shown that the variation in the Jacobian causes the worse performance of the exact optimised rational approximation, whereby the effect of the polynomial in the denominator of the expression in Eq. (4) is to cause excessive distortion of the mappings leading to non-uniform distribution of the vector basis functions in the problem domain.

Tolerance theory [19] predicts errors in the RCS of a scatterer due to errors in the scatterer's geometrical representation. RCS errors are calculated from phase errors introduced by shifting the geometry from the exact scatterer surface. Here it has been shown that a tolerance theory applied to the BEM based on curvilinear patches would need to be extended to include the distortion of the surface parameterisation.

REFERENCES

1. Rao, S. M., D. R. Wilton, and A. W. Glisson, "Electromagnetic scattering by surfaces of arbitrary shape," *IEEE Transactions on Antennas and Propagation*, Vol. 30, No. 3, 409–418, 1982.
2. Wandura, S., "Electric current basis functions for curved surfaces," *Electromagnetics*, Vol. 12, 77–91, 1992.

3. Graglia, R. D., D. R. Wilton, and A. F. Peterson, "Higher order interpolatory vector basis for computational electromagnetics," *IEEE Transactions on Antennas and Propagation*, Vol. 45, 329–342, 1997.

4. Wang, J. and J. P. Webb, "Hierarchal vector boundary elements and p-adaption for 3-D electromagnetic scattering," *IEEE Transactions on Antennas and Propagation*, Vol. 45, No. 12, 1869–1879, 1997.

5. Djordjevic, M. and B. M. Notaros, "Double higher order method of moments for surface integral equation modeling of metallic and dielectric antennas and scatterers," *IEEE Transactions on Antennas and Propagation*, Vol. 52, No. 8, 2118–2128, 2004.

6. Valle, L., F. Rivas, and M. F. Catedra, "Combining the moment method with geometrical modelling by NURBS surfaces and Bézier patches," *IEEE Transactions on Antennas and Propagation*, Vol. 42, 373–381, 1994.

7. Perez, J. and M. F. Catedra, "Application of physical optics to the RCS computation of bodies modeled with NURBS surfaces," *IEEE Transactions on Antennas and Propagation*, Vol. 42, 1404–1411, 1994.

8. Kolundzija, B. M. and B. D. Popovic, "Entire-domain Galerkin method for analysis of metallic antennas and scatterers," *IEE Proceedings H*, Vol. 140, 1–9, 1993.

9. Babuska, I. and A. K. Aziz, "On the angle condition in the finite element method," *Siam Journal on Numerical Analysis*, Vol. 13, No. 2, 214–226, 1976.

10. Hellicar, A. D., J. S. Kot, G. James, and G. K. Cambrell, "Nodal- and edge-based vector basis functions on higher order and rational geometries in the BEM," *IEEE Transactions on Antennas and Propagation*, Vol. 56, No. 4, 2008.

11. Hellicar, A. D. and J. S. Kot, "Nodal- and edge-based vector basis functions on higher order and rational geometries in the BEM," *Proceedings, U.R.S.I. International Symposium on Electromagnetic Theory*, Vol. 42, Pisa, Italy, 2004.

12. Dietz, R., J. Hosheck, and B. Jüttler, "Rational patches on quadric surfaces," *Computer Aided Design*, Vol. 27, 27–40, 1995.

13. Lyness, J. N. and D. Jespersen, "Moderate degree symmetric quadrature rules for the triangle," *J. Inst. Maths Applics*, Vol. 15, 19–32, 1975.

14. Poggio, A. J. and E. K. Miller, *Computer Techniques for Electromagnetics*, Chapter 4, Pergamon Press, 1973.

15. Duffy, M. G., "Quadrature over a pyramid or cube of integrands with a singularity at a vertex," *Siam Journal on Numerical Analysis*, Vol. 19, No. 6, 1260–1262, 1982.

16. Mie, G., "Beiträge zur optik trüber medien, speziell kolloidaler metallösungen," *Ann. Physik*, Vol. 25, No. 3, 377–445, 1908.

17. Mautz, J. R., "Computer program for the mie series solution of a sphere," Tech. Rep. TR-77-12, Syracuse University, Dec. 1977.

18. Mohsen, A. A., A.-R. Helaly, and J. M. Fahmy, "The corrected induced surface current for arbitrary conducting objects at resonance frequencies," *IEEE Transactions on Antennas and Propagation*, Vol. 43, 448–451, 1995.

19. Ruze, J., "Antenna tolerance theory — A review," *IEEE Proceedings*, Vol. 54, 633–640, 1966.